Scientific Research Publishing

Journal of Geoscience and Environment Protection, 2024, 12, 180-210
https://www.scirp.org/journal/gep
ISSN Online: 2327-4344
ISSN Print: 2327-4336

Structural Controls and Predictive Mapping of Tin, Niobium and Tantalum Mineralization Associated with the Mayo Darlé Stanniferous Granitoids; Contributions of Geostatistics

Bah-Yero Liman[1*], Ngounouno Ismaïla[2], Mbowou Gbambié Isaac Bertrand[2], Alpha Baster Kenfack Fokem[2], André William Boroh[2], Amadou Diguim Kepnamou[3]

[1]Department of Earth Sciences, Faculty of Science, University of Ngaoundéré, Ngaoundéré, Cameroon
[2]Department of Mining Geology, School of Geology and Mining and Engineering, University of Ngaoundéré, Meiganga, Cameroon
[3]Department of Earth Sciences, Faculty of Science, University of Garoua, Garoua, Cameroon
Email: *limanbahyero@gmail.com

How to cite this paper: Liman, B.-Y., Ismaïla, N., Bertrand, M. G. I., Fokem, A. B. K., Boroh, A. W., & Kepnamou, A. D. (2024). Structural Controls and Predictive Mapping of Tin, Niobium and Tantalum Mineralization Associated with the Mayo Darlé Stanniferous Granitoids; Contributions of Geostatistics. *Journal of Geoscience and Environment Protection, 12,* 180-210.
https://doi.org/10.4236/gep.2024.121012

Received: November 24, 2023
Accepted: January 27, 2024
Published: January 30, 2024

Copyright © 2024 by author(s) and Scientific Research Publishing Inc.
This work is licensed under the Creative Commons Attribution International License (CC BY 4.0).
http://creativecommons.org/licenses/by/4.0/

Open Access

Abstract

The aim of this study of the spatial dispersion of tin, niobium and tantalum mineralization associated with the Mayo Darlé granitoids was to produce prospecting guides through predictive maps of Sn, Nb and Ta in the region. It was based on a database (in appendix) obtained after analysis of rock samples (greisens and quartz veins) collected in the field, using a portable X-ray fluorescence (XRF) spectrometer. Two approaches were used: 1) structural studies in the field using the directions of veins and fractures 2) the use of variographic maps, an essential element in geostatistics for determining directional anisotropies. A joint synthesis of the modelling results shows that tin, tantalum and niobium mineralization at Mayo Darlé is concentrated along strike intervals N315E to N320E, with mineralization also occurring along strike N35E for high-grade Sn, medium-grade Ta and low-grade Nb. In short, mineral concentrations disperse progressively in space: positively from east to west for tantalum and niobium, and inversely for tin.

Keywords

Mayo Darlé, Tin, Niobium, Tantalum, Geostatistics, Mapping

1. Introduction

Dani Krige's work on statistics applied to the Witwatersrand gold deposit inspired Georges Matheron to use the variogram to estimate deposits. In honor of

this, he gave the name "kriging" to the estimation algorithm at the heart of his regionalized variable theory (Georges M. 1976). Thanks to the rise of computer science and machine learning in particular, geostatistical techniques are increasingly used today in several scientific disciplines (climatology, hydrogeology, agriculture...) to produce predictive maps and/or estimate reserves. As an example, geostatistics has been used to assess contamination and spatial variability, and to provide the prediction maps of the distribution of physicochemical parameters (pH, electrical conductivity and sediment organic matter) and trace metals in surface sediments along the Lom River in the gold mining area of Gankombol (Ayiwouo et al., 2023), to produce the prediction maps of iron content from a drilling campaign carried out in southern Cameroon (Boroh et al., 2022b) and for the spatial distribution prediction for the ground water quality in Mosul City (Iraq) (Ibrahim & Al-Tamir, 2023). In this work, we have chosen to use the same method to carry out predictive mapping of Sn, Nb and Ta mineralization associated with the Mayo Darlé granitoids.

The Mayo Darlé tin deposit was discovered in 1927 and was intensively mined (alluvial and eluvial) from 1933 to 1986 (Gweth, 2011). It is located on the northern and northeastern flanks of the intrusive Guengué granite massif, assimilated to the younger stanniferous granites of Nigeria. Since then, several studies have been carried out in the region, including those by Nguene (1982) and BRGM (1986). Among other things, these studies revealed the mineral paragenesis of Mayo Darlé cassiterite, the existence of other minerals such as columbite-tantalite, and an estimate of residual alluvial and eluvial tin reserves. However, no systematic study has been carried out on the lateral and/or depth extension of the primary ore, which is the priority target in the region. We have therefore chosen to produce a predictive map illustrating the spatial dispersion of tin, niobium and tantalum from a database obtained after portable X-ray fluorescence (XRF) analysis of rock samples collected in the field. The aim of this work is to produce prospecting guides for more in-depth future work.

2. Geological Context

The Mayo Darlé anorogenic plutonic complex is an alignment of elliptical granite massifs intrusive into the Pan-African basement. It has been the subject of several geological and mining studies since the discovery of the region's tin deposit. These studies show that the region is essentially made up of biotite gneisses and quartz metadiorites dated at 614 ± 20 Ma (Rb-Sr), biotite and hornblende gneisses, garnet gneisses and granites dated at 65 ± 12 Ma by the Rb-Sr method (Gazel et al., 1963). It is located on the Cameroon hot line (**Figure 1**) and is one of around twenty anorogenic ring massifs on the Adamaoua plateau. The Cameroon hot line (Ngounouno, 2013) is a N 30˚E alignment of oceanic and continental volcanic edifices from Pagalu Island to Lake Chad (Gèze, 1941) and continental anorogenic plutonic complexes. It has been tectonically active since the Precambrian (Moreau et al., 1987), but magmatic activity has only developed

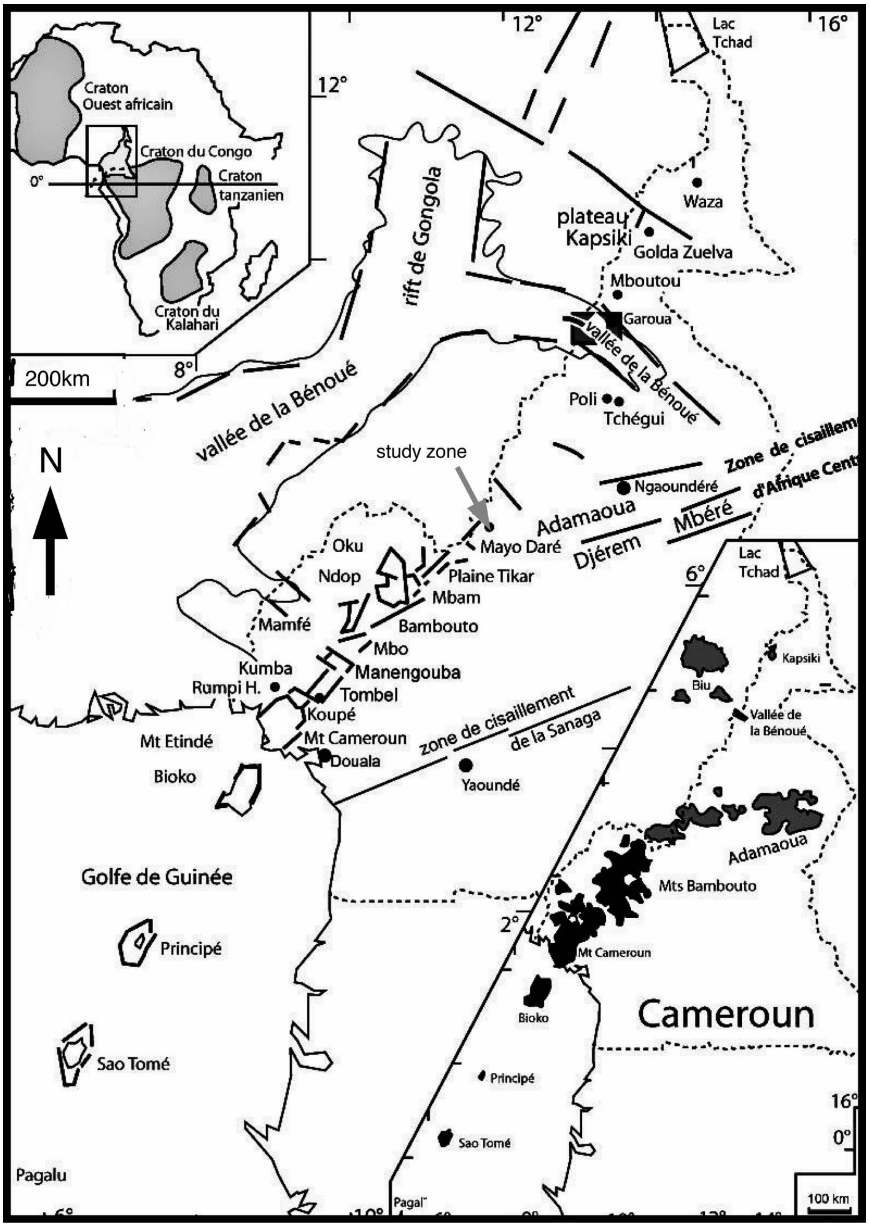

Figure 1. The Cameroon hot line extends from Pagalu Island to Lake Chad, between the West African and Congo cratons (upper cartouche after Kampunzu and Popoff, 1991).

since the fin of the Cretaceous and began with the emplacement of annular plutonic complexes. These complexes are more abundant to the south (between Foumban and Banyo) than to the north of the continental part of the Cameroon hot line. They are modest in size (5 to 10 km in diameter) and were emplaced between the Paleocene (66 Ma) and Lower Oligocene (33 Ma) (Lasserre, 1978). The Adamaoua plateau is made up of four major volcanic complexes: the volcanic massifs of Tchabal Nganha (Nono et al., 1994), Tchabal Djinga (Ézangono et al., 1995), Tcbabal Mbabo (2640 m) and the volcanic zone to the north, east and south of Ngaoundéré (Déruelle et al., 1987; Nkouandou et al., 2006). Molybdenum, tungsten, fluorite, niobium, tantalum and gold constitute the minera-

lization associated with the Cameroon hot line (Laplaine, 1969).

3. Methodology

Predictive mapping makes it possible to rapidly target zones that are a priori favorable for the discovery of deposits, and thus to reduce exploration costs and lead times. It involves interpolating a number of points of known grade over an entire area, using a two-dimensional estimation model. In this way, geostatistics offers an advantage over conventional estimation methods, by taking into account the spatial structure of the phenomenon under study. To achieve this, the work was carried out in three main phases:

1) The field phase, which consisted of:

Study of the structural elements affecting the geological formations in the study area, as well as the ore bodies;

Systematic sampling of quartz and greisen veins from artisanal mining sites. 75 samples were selected for spectrometer analysis.

2) The laboratory phase, during which each sample was analyzed using an Olympus delta premium portable XRF spectrometer equipped with a large SDD detector and an X-ray tube with a 4 W, 200 μA (max.) anode, with optimized beam settings.

Analysis principle: X-rays from the analyzer are bombarded onto a selected surface of the rock. The result, in percentage of chemical elements, is read directly from the screen of the analyzer, whose calibration is preset at 35 seconds. The analytical results of these samples were downloaded from the analyzer and recorded in an Excel file.

3) Data processing, analysis and interpretation.

This is the crucial stage of the study, as generally the database containing the results of chemical analyses contains either additional information not useful for the work, or missing values rejected by the estimation software, or a heap of information to be increased or reduced (Rossi & Deutsch, 2013). As operations to be carried out, we proceeded:

a) Treatment of missing data and unquantified values; for two-dimensional geostatistical estimation, three attributes are used, the two coordinates X and Y for longitude and latitude and the value to be estimated (Reza et al., 2010), in this case one of the three elements mentioned above. For each trio of elements, there must be no missing value. In the database, these incomplete lines have been removed;

b) Adding data: As the samples were only taken from artisanal logging sites, the sampling carried out is not representative of the entire region and needs to be completed. In order to perfect this, we use data obtained in the field and the work of Nguene (1982) in the north-eastern part before proceeding with data augmentation. This is a very recurrent operation in data analysis, which consists in completing an incomplete database with an estimate (Maharana et al., 2022). An irregular grid of 100 points was created within the domain under study, and

the augmented data were interpolated using an adapted algorithm.

c) Model formulation: To formulate a model in line with the phenomenon represented by the regionalized random variable, a thorough exploration of the data is essential. Based on the results of this descriptive analysis, the type of model and kriging is chosen judiciously and the variographic analysis carried out in a more enlightened way. In this study, work is carried out using two approaches: ordinary kriging and machine learning. A cross-validation will be performed to select the best model at the end.

- Analysis and modeling of spatial structure

Any geostatistical study is often preceded by a variographic analysis, which involves assigning a variogram model to known observations. The variogram is the ideal tool for describing regionalized variables.

- Variogram analysis

The application of kriging (Figure 2) presupposes knowledge of the spatial

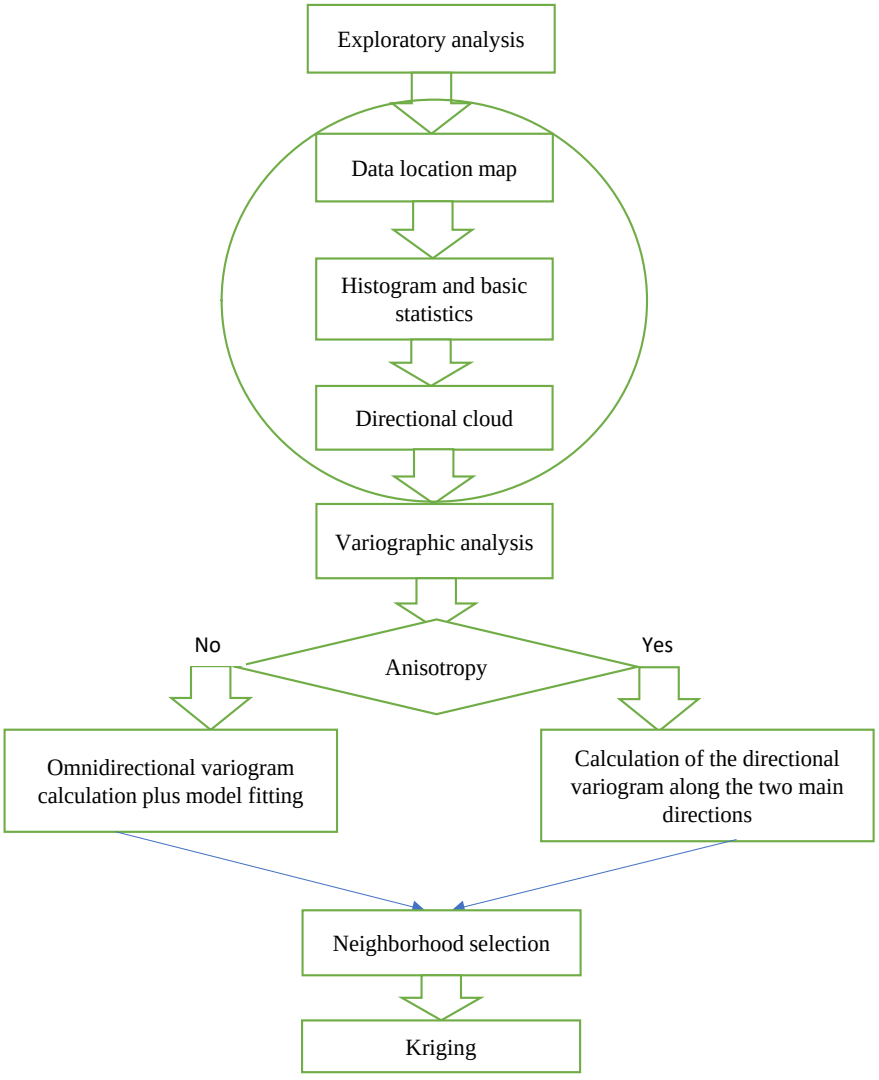

Figure 2. Ordinary kriging implementation.

structure of the random function. In practice, however, this is rarely known. Variational analysis is a prerequisite for kriging, enabling it to be estimated (Baillargeon, 2005). This analysis is in fact the study of the spatial behavior of the regionalized variable in question. In this case, where the representation of the regionalized variable is stationary, we consider a function representing spatial dependence: the variogram or semivariogram is defined by the following relationship:

$$y(h) = \frac{1}{2} * E\left[Z(x) - Z(x+h)\right]^2 \quad (1)$$

This relationship gives the theoretical value of the variogram. In nature, however, we only have the experimental variogram calculated from pairs of points, to which a theoretical model must be fitted. For a given value h, we obtain an estimate of the variogram of (h) as follows.

Let $N(h)$ be the set of pairs (x_i, x_j) of measurement sites such that $x_i - x_j = h$ and $|N(h)|$ = Card ($N(h)$) then,

$$y^*(h) = \frac{1}{2|N(h)|} \sum_{(x_i, x_j) \in N(h)} \left[Z(x) - Z(x+h)\right]^2 \quad (2)$$

Once the experimental variogram has been calculated, it will be fitted by a predefined model.

At the end of these operations, a sampling map showing the data to be used for predictive mapping was produced (Figure 3).

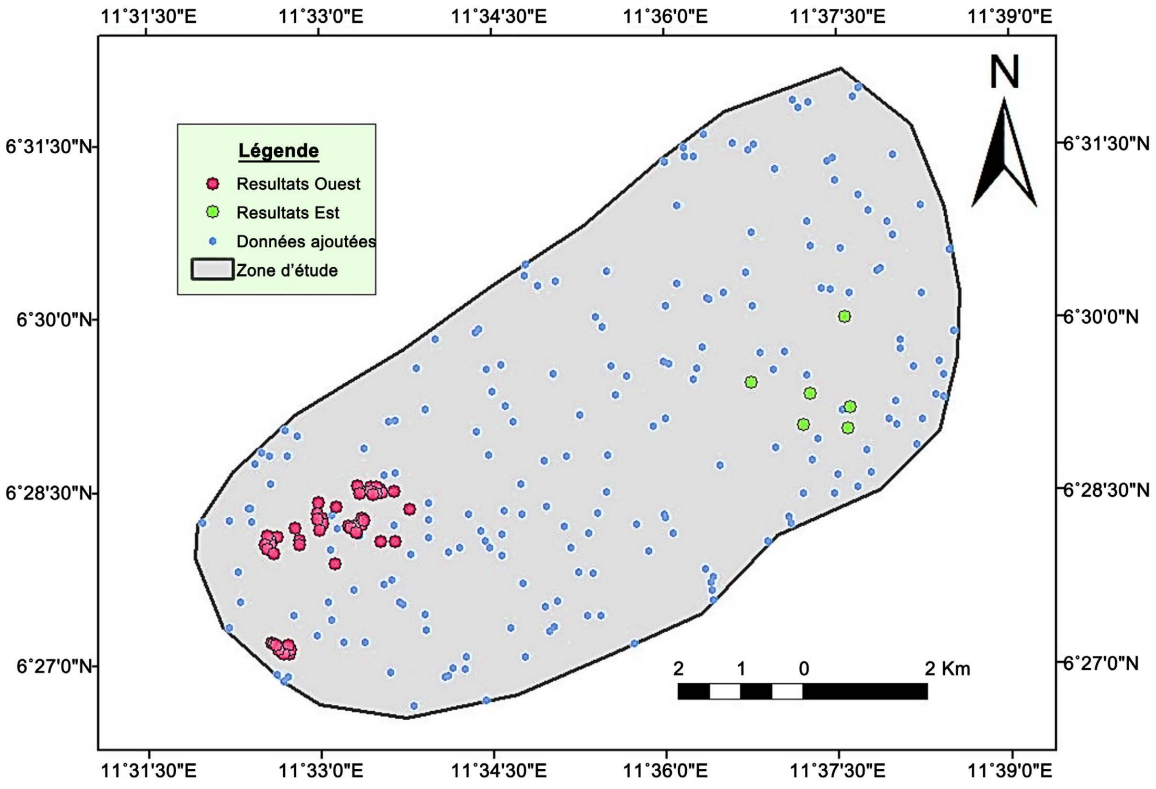

Figure 3. Estimation sampling map.

4. Results and Discussion

This map shows a differentiation between sample analysis results (in red), literature data (in green) and augmented data (in blue).

4.1. Basic Statistical Analysis

Statistical analysis was carried out on the basic data. As a first step, statistical calculations were performed to characterize the data (Table 1).

The histogram of tin values (Figure 4) follows a log normal distribution with a mean of 0.059% and a standard deviation of 0.157%. The coefficient of variation is 266.10%. The maximum value is 2.06% and the minimum is 0.01% (Table 1). The histogram is unimodal, with the lowest values (below 0.1%) having the highest frequencies (83%). This explains the dominance of the lowest values (<0.1%).

The niobium histogram follows a log normal distribution with a mean of 0.019% and a standard deviation of 0.011% (Figure 5). The coefficient of variation is 0.59%. The histogram is unimodal. There is an irregularity in the interval [0.2%; 0.21%] characterizing samples with high niobium contents. From this graph, we can divide Nb mineralization into two main groups:

Table 1. Exploratory analysis of Sn, Nb and Ta geochemical data.

Variables (%)	Minimum	Maximum	Moyenne (m)	Écart-type (σ)	Coefficient de variation (σ/m)
Sn	<0.01	2.06	0.059	0.157	0.26
Nb	<0.01	0.06	0.019	0.011	0.59
Ta	<0.01	0.03	0.012	0.004	0.32

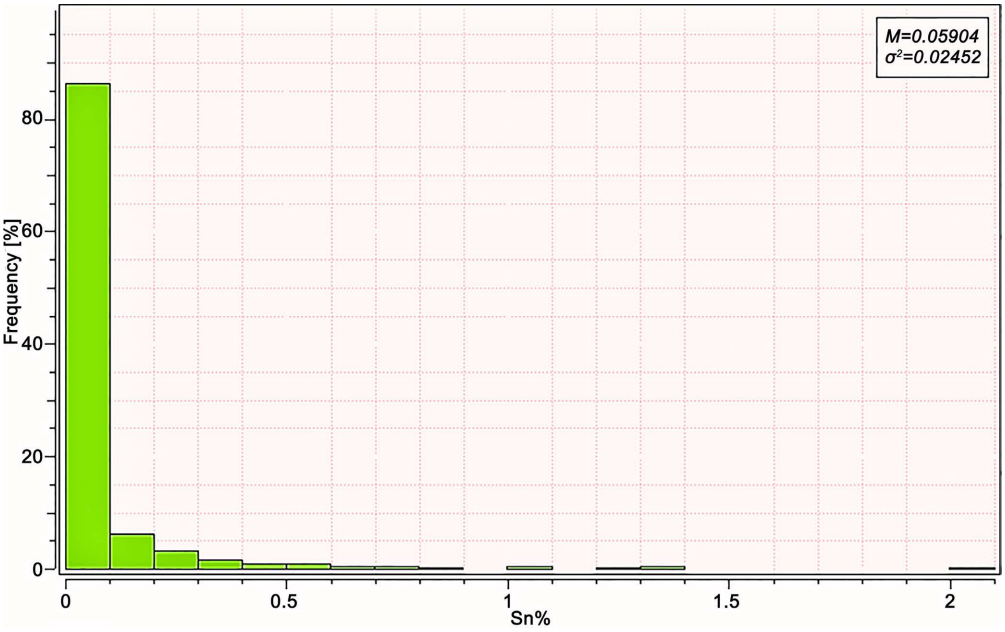

Figure 4. Histogram of tin values.

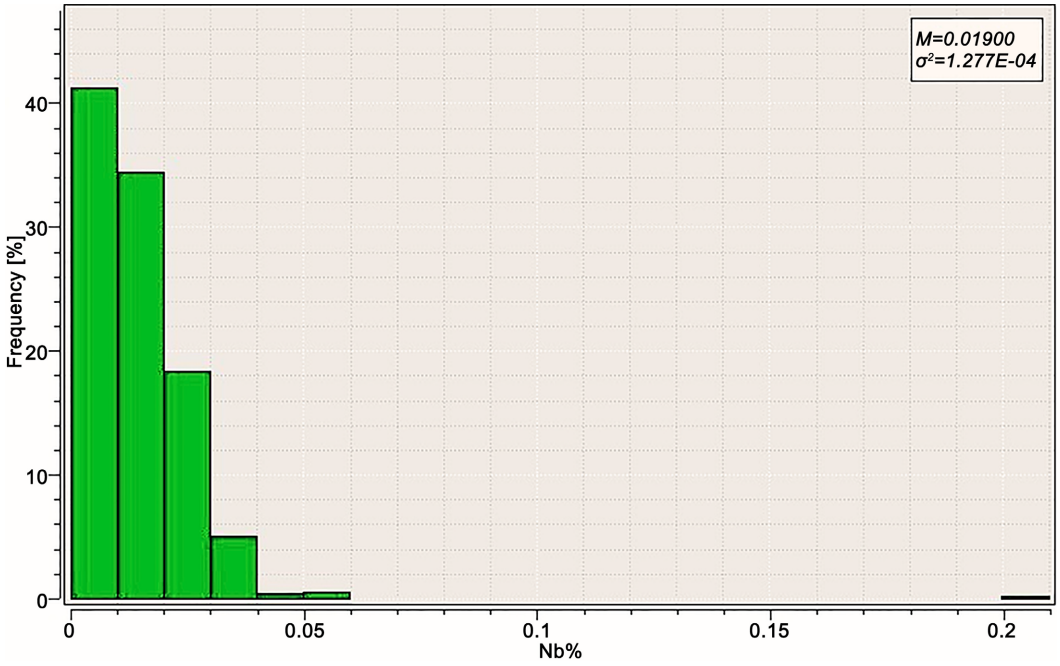

Figure 5. Histogram of Niobium values.

- Zone 1 with niobium grades between 0.01 and 0.06%;
- Zone 2, with niobium concentrations above 0.2%.

Over 95% of samples have a niobium content of less than 0.2%. This explains the dominance of lower values (<0.2%).

The histogram of tantalum values also follows a log normal distribution with a mean of 0.012% and a standard deviation of 0.004% (**Figure 6**). The coefficient of variation is 0.32%. The histogram is unimodal. From this graph, we can divide Ta mineralization into 04 major zones:

- Zone 1 with tantalum grades between [0.01%; 0.012%[;
- Zone 2 with tantalum grades between [0.012%; 0.014%[;
- Zone 3 with tantalum concentrations between [0.014%; 0.018%[;
- Zone 4 with tantalum concentrations [0.019%; 0.025%[.

25% of samples have a tantalum content greater than 0.01. This explains the dominance of low grades (<0.01%).

The main points to emerge from the exploratory analysis of the above data are as follows.

The three histograms produced follow a log normal trend like that of gold ore (Emery, 2001). The estimator used should take into account the Gaussian normal transformation to avoid diluting the weakest data (Glacken et al., 2001).

The presence of multiple geochemical domains on these histograms; for a good estimation study, the histogram must be grouped, in the case of the presence of certain values far removed from the others, we speak of outliers (Barnett et al., 1994). These outliers are detrimental to the estimation process, as they absorb weak values and thus bias grade estimates. They are often caused either by errors in the database or by lithological intrusions. To correct these errors, we

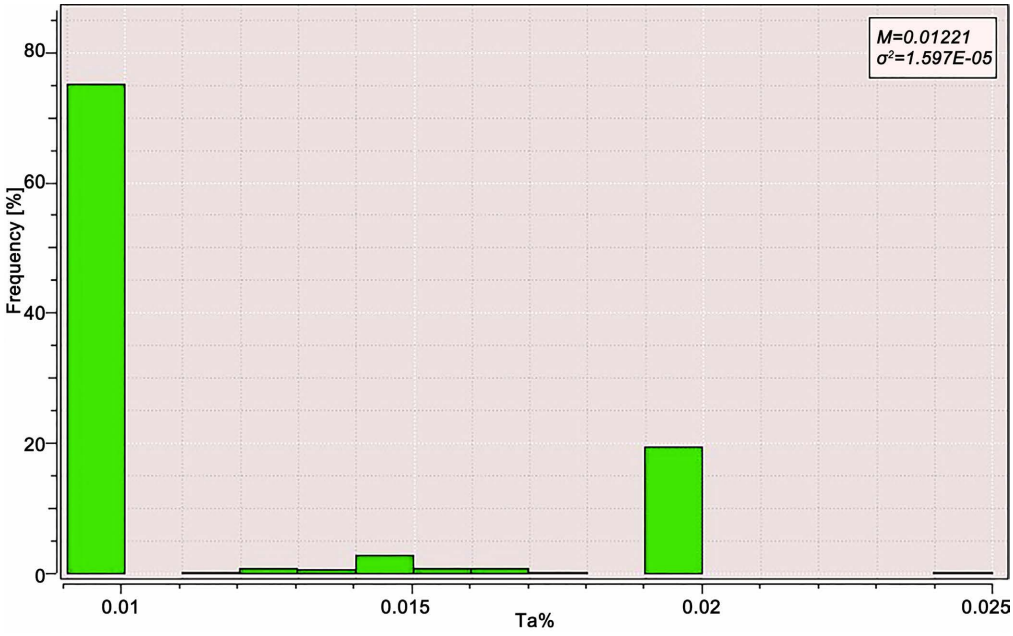

Figure 6. Histogram of tantalite values.

either perform a homogenizing transformation or remove them. In the present case, it is impossible to apply either method, as the aim of predictive mapping is to detect anomalous zones, i.e. those with high concentrations of tin, niobium and/or tantalum.

4.2. Variographic Analysis and Mapping

Geostatistics offers an advantage over conventional estimation methods by taking into account the spatial structure of the phenomenon under study (Chilès & Delfiner, 2012). The mapping of ores such as gold, tantalum, niobium etc. is virtually dependent on this structure, given their mode of formation (Boroh et al., 2022b). In the case studied, there are two options as to preferential direction:

- Structural field studies using vein and fracture directions;
- The use of variographic maps, an essential element in geostatistics for determining directional anisotropies (Calder & Cressie, 2009).

4.3. Field Data Approach

The basement of the Mayo Darlé locality has been affected by several ductile (foliation, schistosity, lineation, folds) and brittle (fractures, veins and shears) deformation structures of varying attitudes. Based on the parallelism of structural elements and the principle of overlap, a relative chronology has been established. These structures can be grouped into four (04) main deformation phases designated D1, D2, D3 and D4 in chronological order of appearance. Each of these deformation phases is characterized by structures visible in the field.

4.3.1. D1 Deformation

The first phase of D1 deformation is evident in the metamorphic rocks (biotite

gneiss and amphibole-biotite gneiss) outcropping in the study area. It is responsible for the formation of foliation S1, which is the only structure belonging to D1 that can be recognized in the field.

The S1 foliation is observed on outcrops in the Mbal Yara, Mayo Darlé and Mayo Seni streams.

In biotite and amphibole-biotite gneisses, the S1 foliation is materialized at outcrop scale by rubbings, i.e. alternating light quartz-feldspathic and dark "beds" rich in ferromagnesian minerals (Figure 7). It is oriented NE-SW (N35E) with an average dip of 41˚NNW (Figure 8(a)).

4.3.2. D2 Deformation

The D2 deformation phase is the most marked in our study area, as it is identified in all metamorphic rocks and is responsible for the development of several structural features (S2 schistosity, L2 lineation, B2 boudins, P2 folds and C2 shear bands).

1) S2 schistosity

This has been identified in virtually all metamorphic rocks and results from the tectonic transposition of the S1 foliation.

In the Mayo Mbal Yara biotite gneiss, S1 is partially or totally transposed into S2 (Figure 9). The latter is of the compositional bedding type, marked by a millimetric to centimetric alternation of light quartzo-feldspathic and dark biotite-rich beds. The minerals in these beds are oriented parallel to the schistosity. The S2 has a major strike N35E (Figure 10(a)) with an average dip of 84˚SE (Figure 10(b)).

In the Mayo Dala amphibole-biotite gneiss, S1 is completely transposed by S2. The latter is underlined by sub-vertical planes of schistosity (Figure 10(b)). The S2 in this gneiss has a major strike N35E (Figure 11(a)) with an average dip of 84˚SE (Figure 11(b)).

2) B2 boudinage

In the study area, boudinage affects the S1 foliation in the biotite gneiss of the Mbal Yara and Mayo Darlé streams (Figure 12). These boudins vary in size (3 to 6 cm long axis and 1 cm to 2 cm short axis), with local concentrations of quartzo-feldspathic material. The boudinage is due to NNW-SSE stretching.

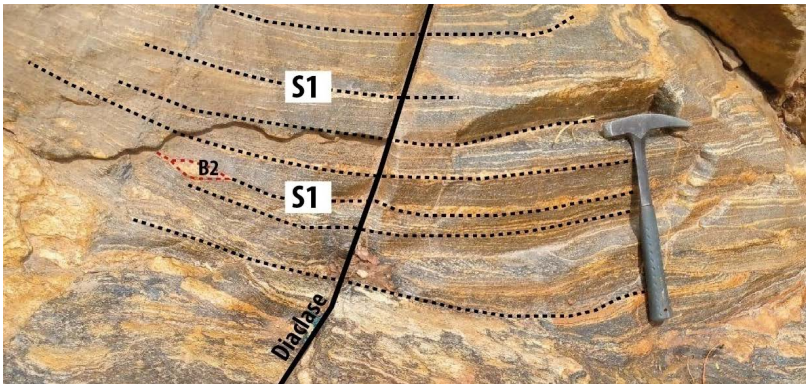

Figure 7. S1 foliation in the Mbal Yara biotite gneiss.

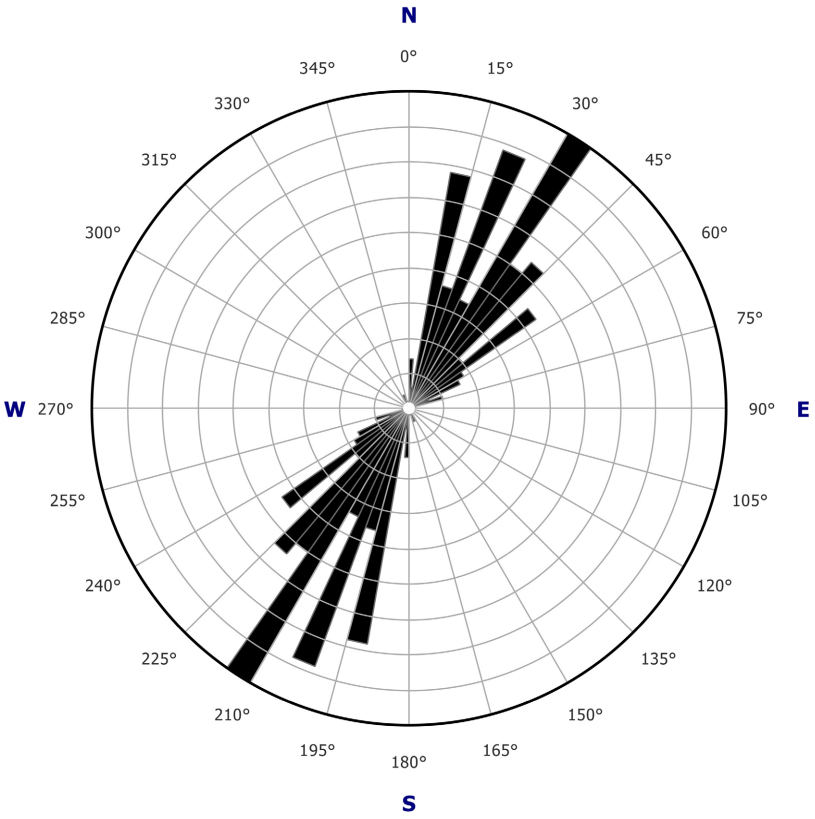

(a)

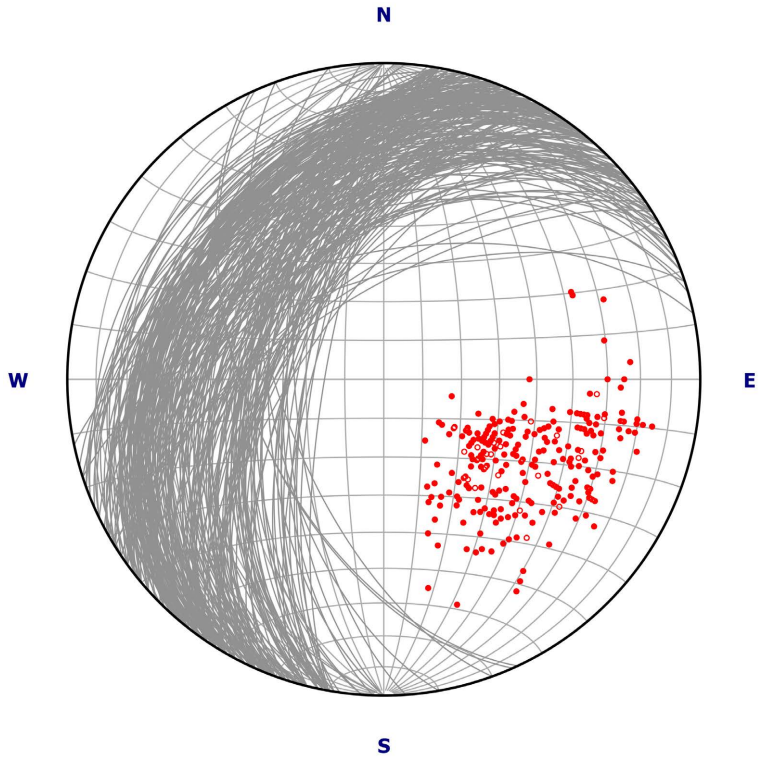

(b)

Figure 8. Stereographic representation of S1 foliation planes (a) directional rosette; (b) stereogram.

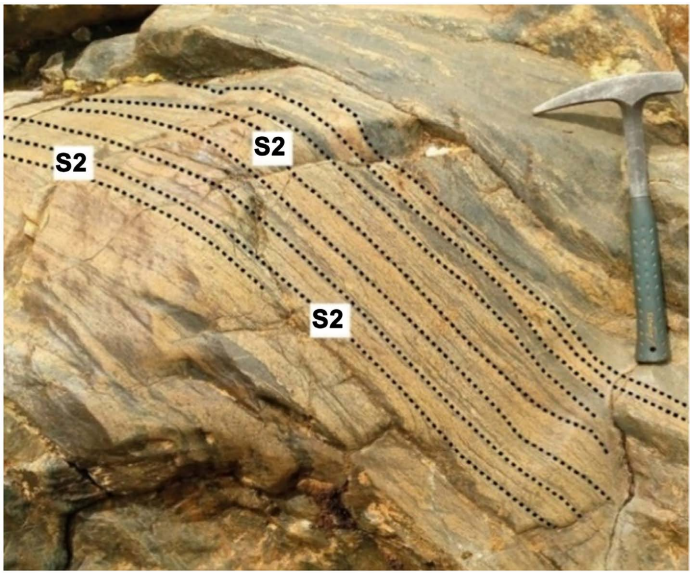

(a)

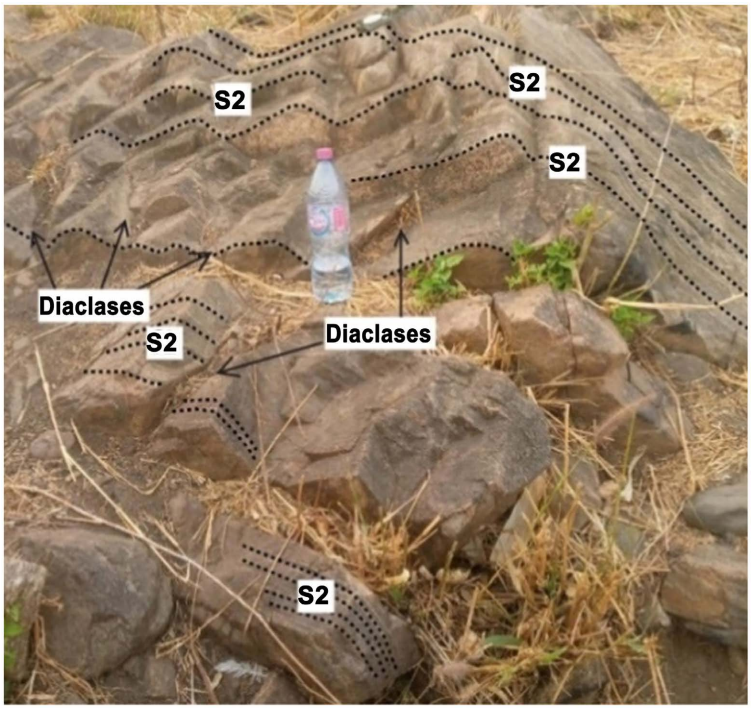

(b)

Figure 9. S2 schistosity in biotite gneiss (a) and amphibole-biotite gneiss (b).

3) L2 lineations

Lineation L2 is found exclusively in the biotite gneiss of the Château district. It is both stretched by the S1 schistosity planes and marked by the stretching of the quartzo-feldspathic strips (**Figure 13**). The stereographic representation of this spatial relationship between L2 and S1 is illustrated by the stereogram in (**Figure 14(a)**). The L2 lineations have a major direction between N10E and N135E (**Figure 14(b)**) and an average dip of 35˚NW.

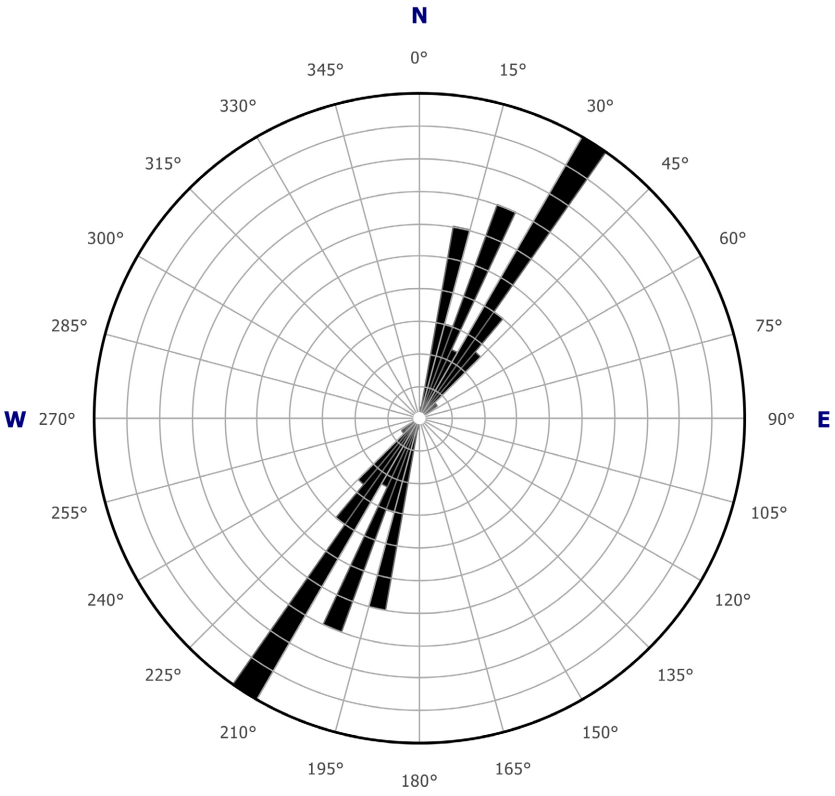

(a)

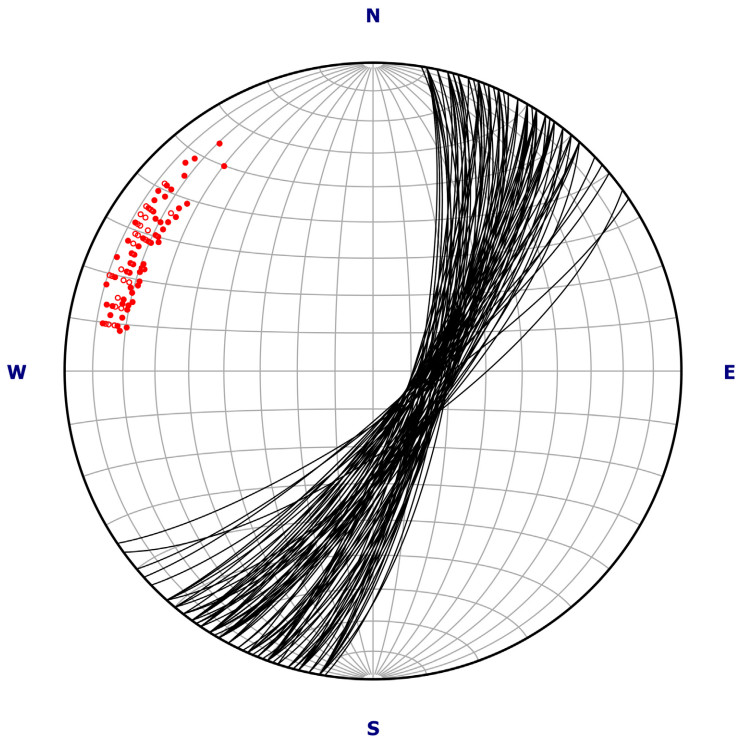

(b)

Figure 10. Stereographic representation of S2 schistosity planes in biotite gneiss (a) directional rosette; (b) stereogram.

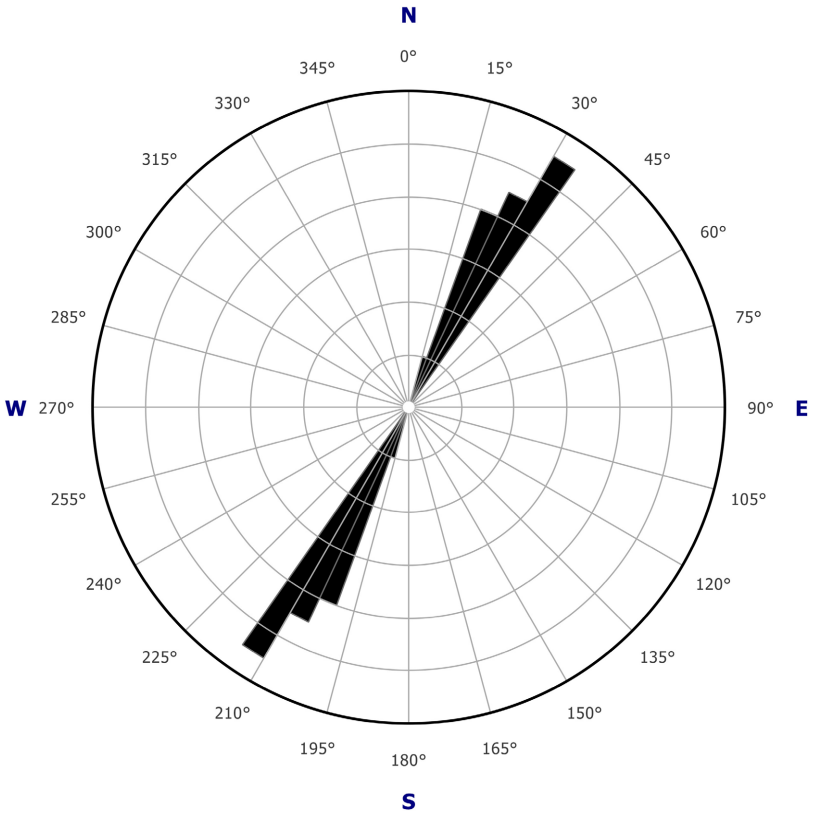

(a)

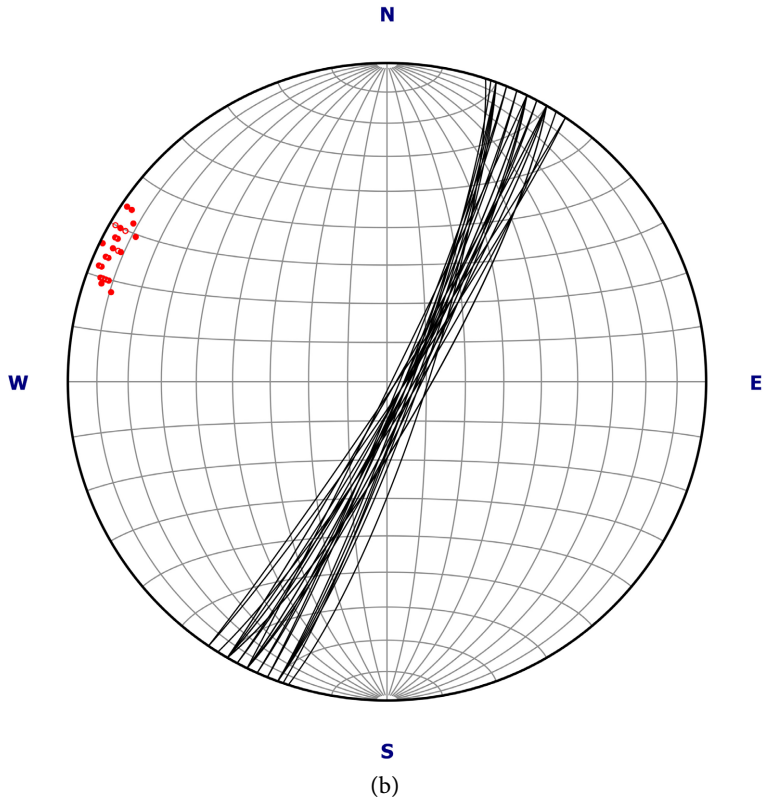

(b)

Figure 11. Stereographic representation of S2 schistosity planes in amphibole-biotite gneiss ((a) directional rosette; (b) stereogram).

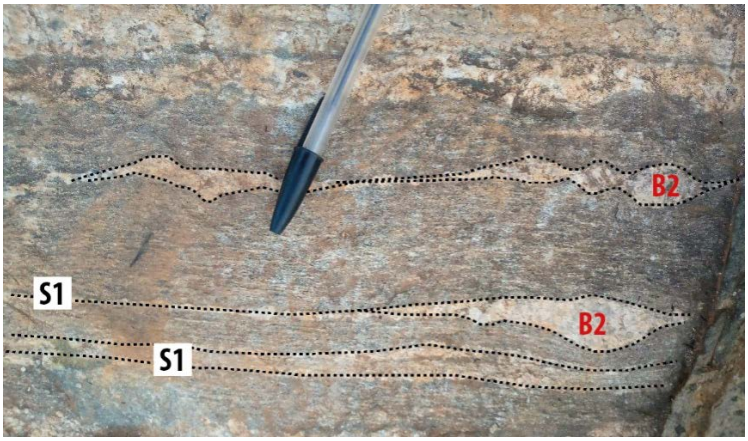

Figure 12. B2 boudinage affecting the S1 foliation in the biotite gneiss.

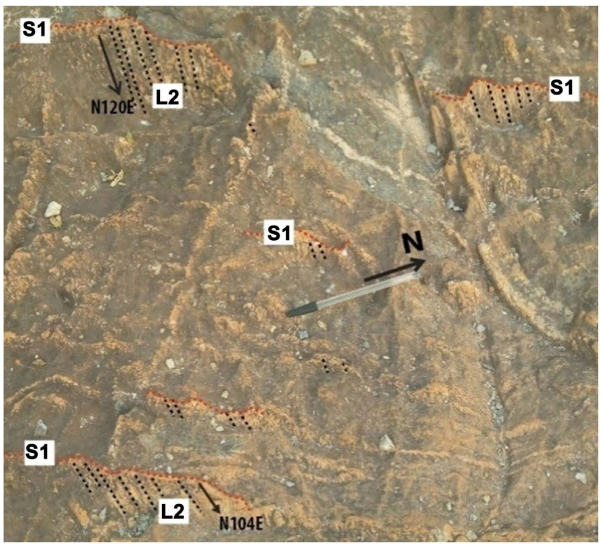

(a)

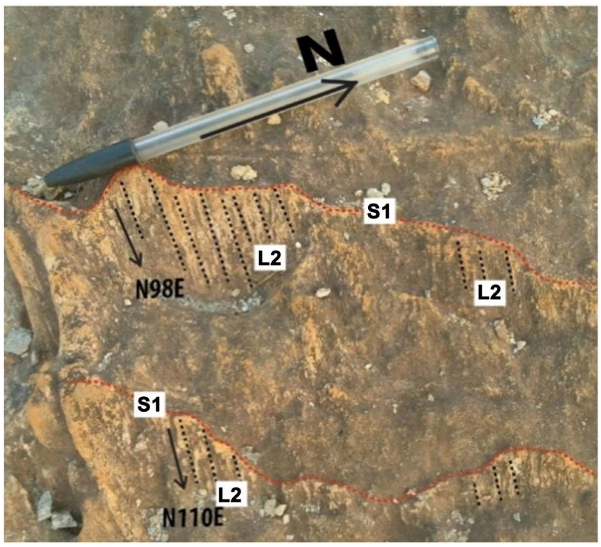

(b)

Figure 13. L2 stretching lineation in a biotite gneiss.

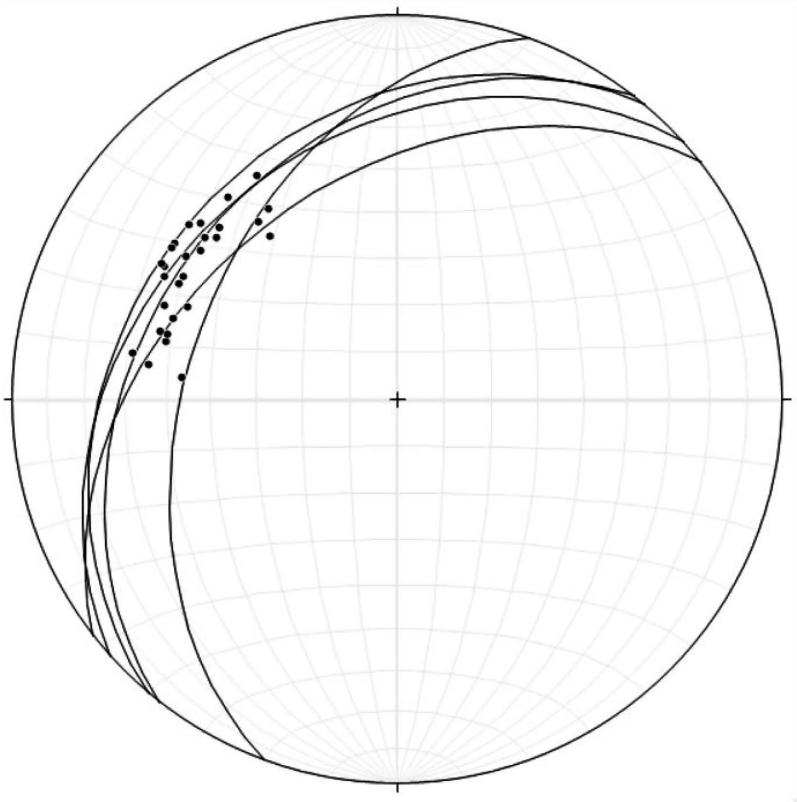

(a)

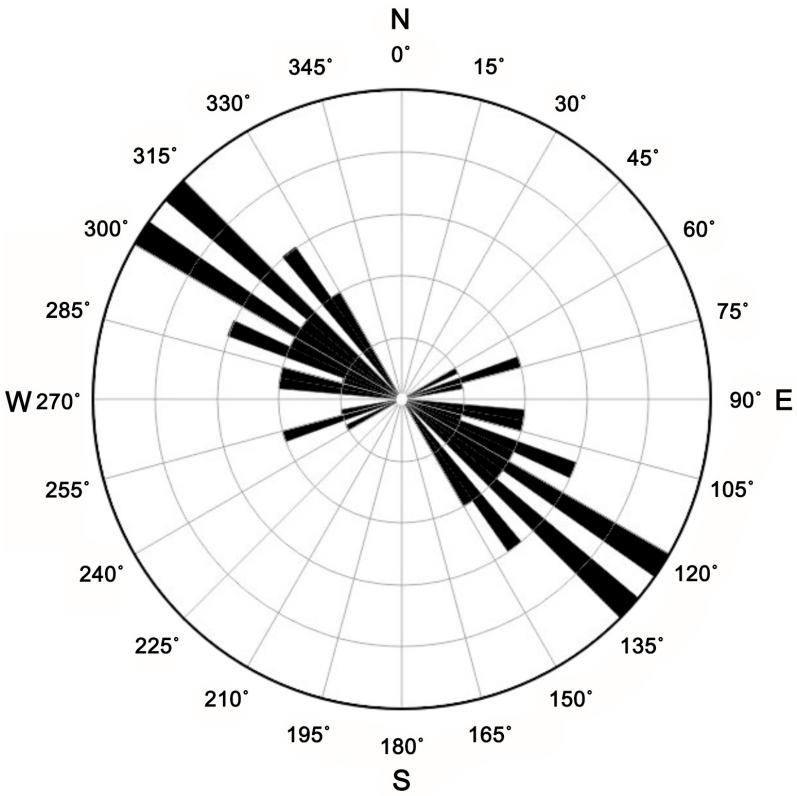

(b)

Figure 14. Stereogram of L2 lineations carried by S1 schistosity planes.

4) P2 folds

P2 folds are frequently found in gneisses. They result from folding of the S1 foliation (Figure 15(a)) in the Mbal Yara biotite gneiss and of the quartzo-feldspathic beds (Figure 15(b)) in the amphibole-biotite gneiss. In the biotite gneiss, the P2 fold (Figure 15(a)) is characterized by a subhorizontal axial plane (recumbent fold) and is generally anisopaque (Figure 15(a)). In the amphibole-biotite gneiss, the quartzo-feldspathic beds are affected by parasitic folds, which are the Z and S folds on the normal flank (Figure 15(b)).

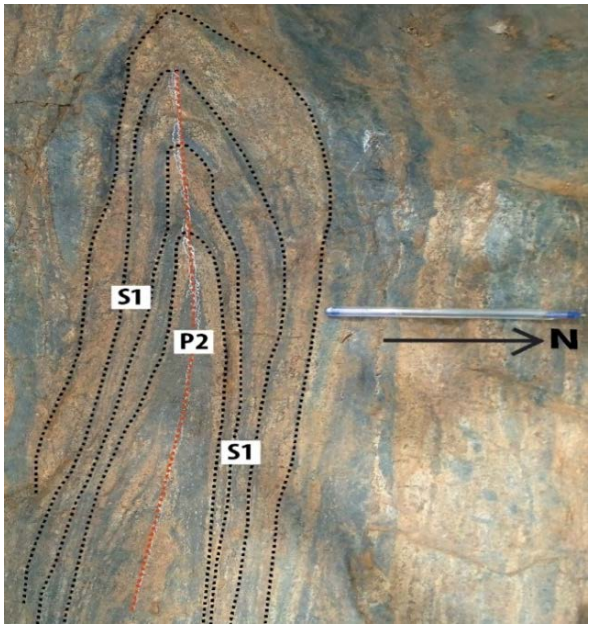

(a)

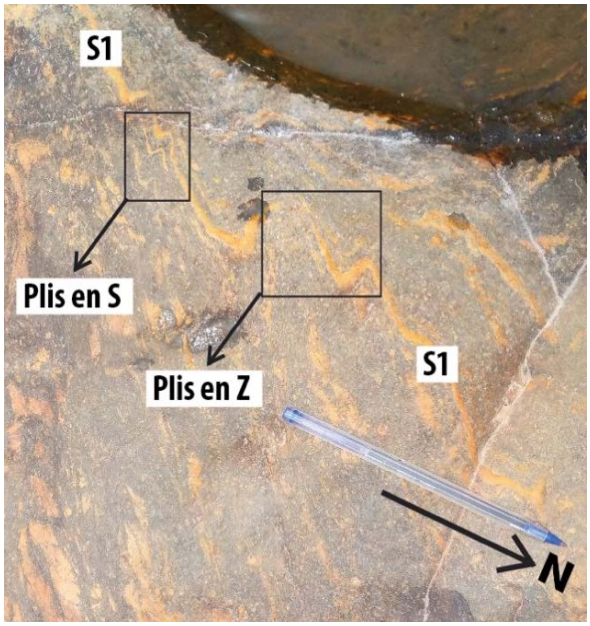

(b)

Figure 15. Anisopaque fold in biotite gneiss (a) and parasitic fold in amphibole gneiss (b).

5) C2 shear bands

C2 shear bands are found only in the Mayo Seni biotite gneisses. They result from the deformation of the S1 foliation on either side of the ductile C2 shear band, thus defining a composite S1/C2 surface (Figure 16). At the point of contact with C2, the S1 foliation is inflected or curved. The overall direction of movement expressed along these shear bands is dextral along a direction N120E.

4.3.3. D3 Deformation

The D3 deformation phase is responsible for setting up new structures (C3 shears and J3 joints).

1) C3 shear

C3 shears, or dropouts, occur in almost all metamorphic rocks. They affect C2/S1 shear bands (N08E) in biotite gneiss along a N102E direction and with dexterous movement (Figure 17). C3 planes may be dry or fed by quartz veins.

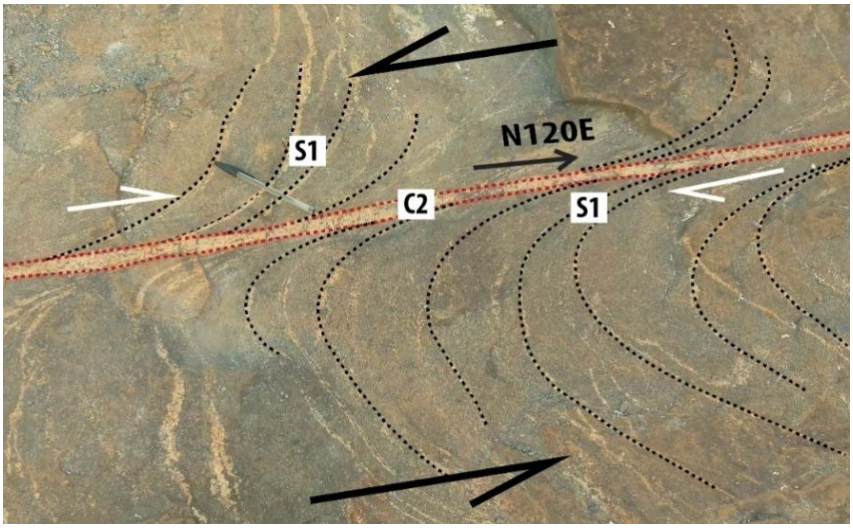

Figure 16. C2/S1 ductile shear band.

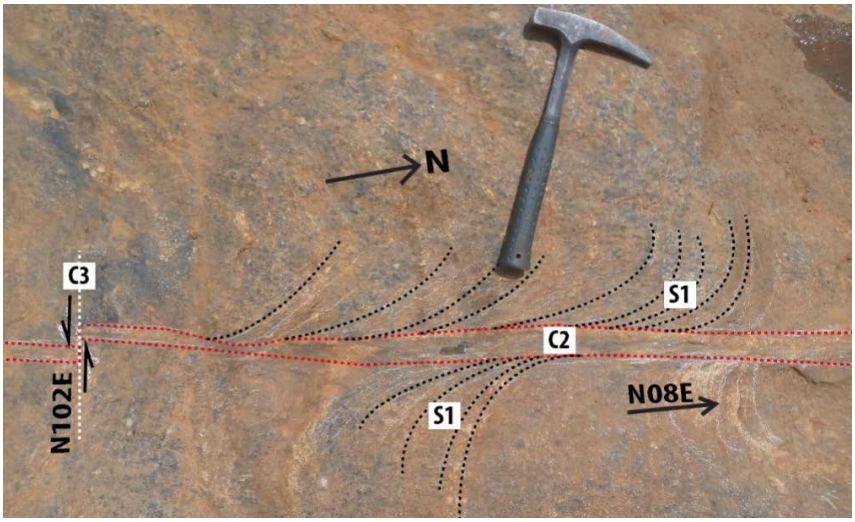

Figure 17. C3 shear affecting a C2/S1 shear band.

2) J3 joints

Joints are found in all lithological types. They are either dry, called diaclases (Figure 18(a)), or filled with quartzo-feldspathic material (Figure 18(b)), or volcanic material (dolerites) (Figure 18(c)). The emplacement of these joints affected the structural elements of phases D1, D2 and D3 in varying directions. Measuring the attitudes of 800 diaclase planes, 50 veins and 30 dolerite dykes in the area's formations has yielded the following major directions: N130E (Figure 19(a)), N15E and N45E (Figure 19(b)), N110E (Figure 19(c)).

4.3.4. D4 deformation

The D4 deformation phase saw the installation of Boudins B4 and shears C4.

1) Boudin B4

A second episode of B4 boudinage affected the elements of D3 deformation (quartz and quartz-feldspar veins) in the granites and gneisses of the study area. This boudinage is incomplete in the amphibole-biotite gneiss (Figure 20(a)) and complete in the quartz veins of the granites (Figure 20(b)). These boudins vary in size from 6 to 10 cm for the long axis (elongation axis) and from 1 to 6cm for the short axis (stretching axis).

(a)

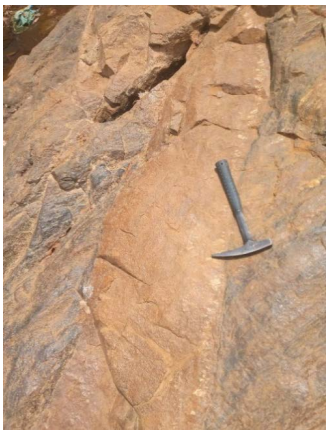

(b)

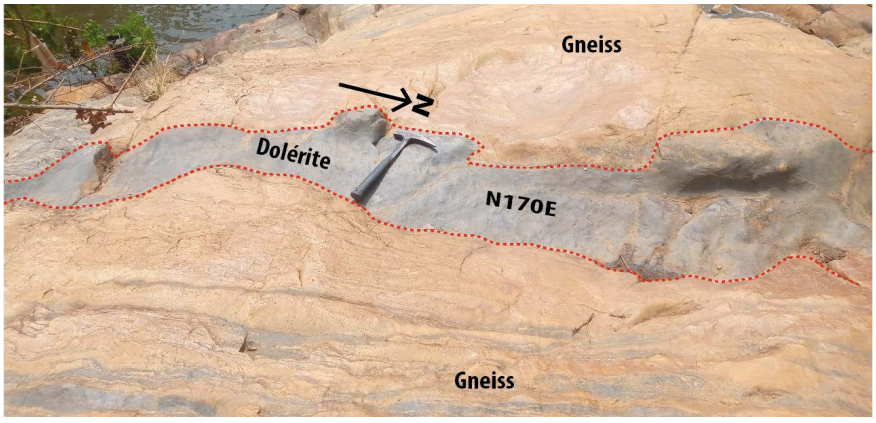

(c)

Figure 18. Elements of the D3 deformation ((a) diaclases in dolerite; (b) quartzo-feldspathic threads in amphibole gneiss; (c) dolerite dyke in biotite gneiss).

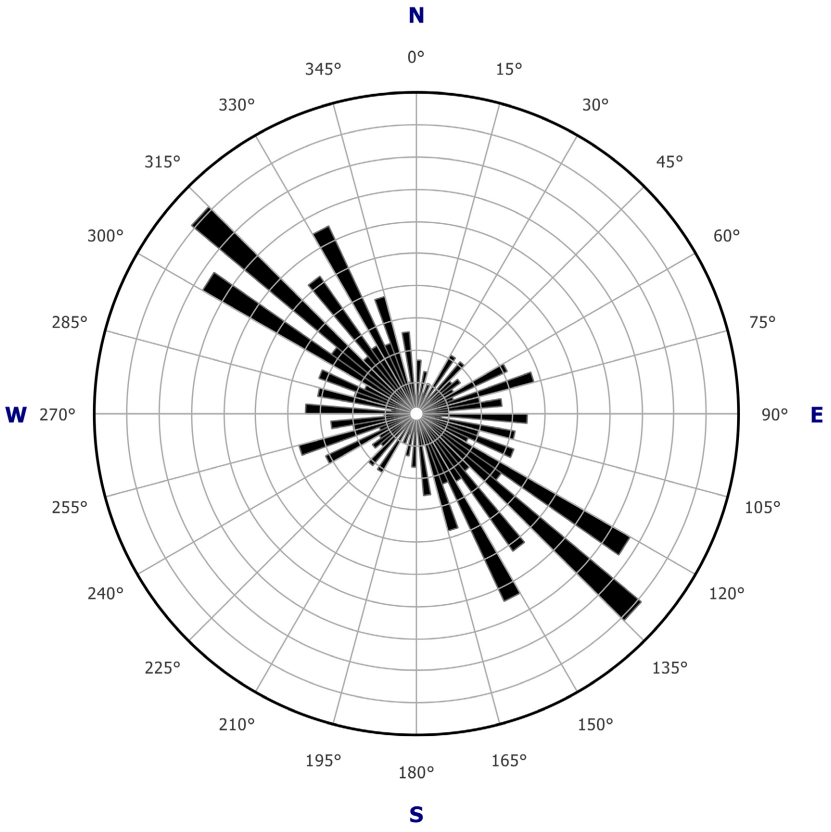
N
0°
15°
30°
45°
60°
75°
90°
E
105°
120°
135°
150°
165°
180°
195°
210°
225°
240°
255°
W
270°
285°
300°
315°
330°
345°
S

(a)

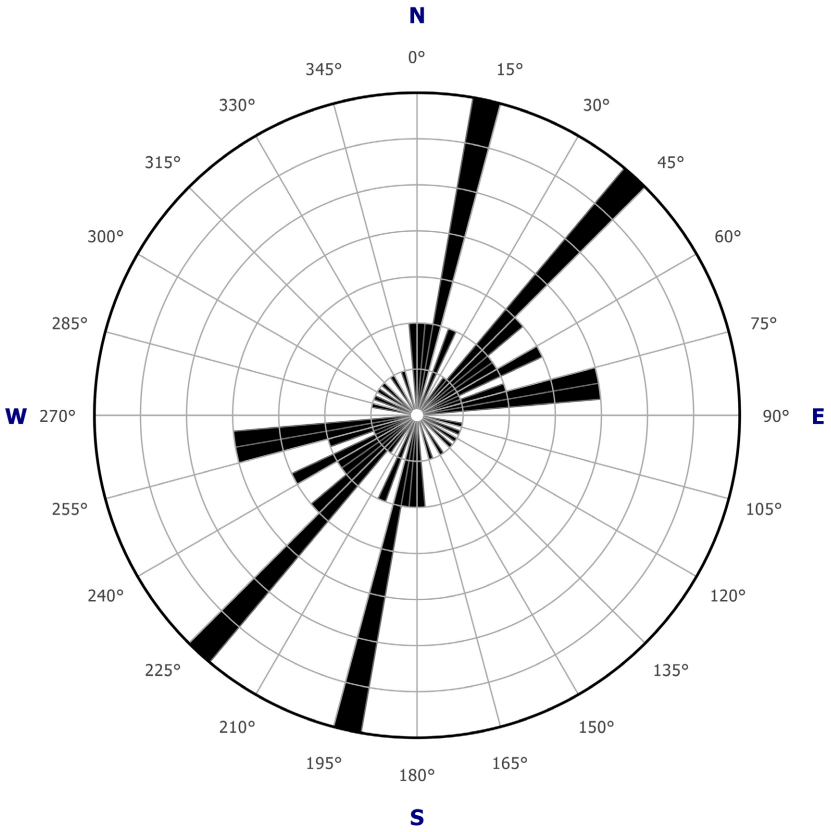
N
0°
15°
30°
45°
60°
75°
90°
E
105°
120°
135°
150°
165°
180°
195°
210°
225°
240°
255°
W
270°
285°
300°
315°
330°
345°
S

(b)

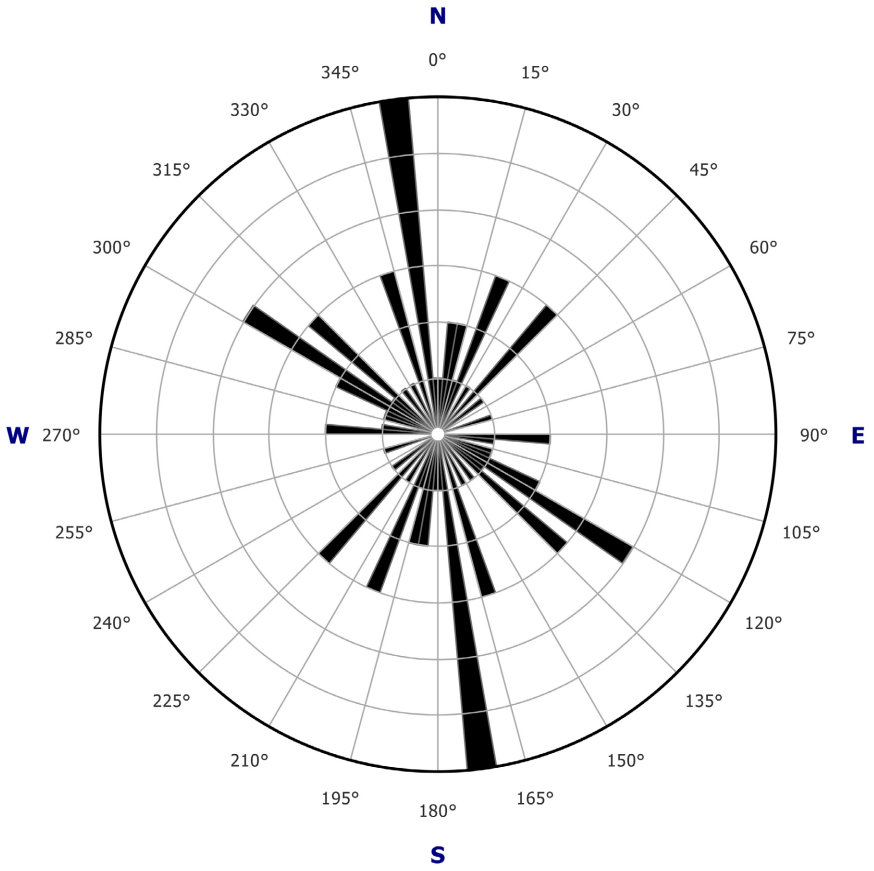

(c)

Figure 19. Directional rosette of joint elements ((a) diaclases; (b) threads and veins; (c) dolerite dikes).

2) C4 shears

The second episode of brittle C4 shearing (unconformity) affected the quartzo-feldspathic veins of the D3 deformation contained in the biotite gneiss (Figure 21(a)) and in the amphibole-biotite gneiss (Figure 21(b)). It is more developed in the biotite gneiss along directions N60E and N70E and affects a series of veins oriented N10E with a dextral direction of movement (Figure 21(a)). In the amphibole-biotite gneiss, on the other hand, it affects a vein following a N50E strike with sinister movement (Figure 21(b)).

4.4. Geostatistical Approach Using Geochemical Data

This approach is based on the value of the variogram. This method is derived from the principle of continuity of mineralization, which states that two bodies of the same nature have the same geochemical composition, so if the variogram value calculated between two points is low, there is a good chance that their supports are of the same nature (Emery, 2001). The tool used to show this continuity is the variogram map. Figure 22 shows the variogram map produced in the study area.

On this map, a major direction is observed on N315E. This is the zone with

(a)

(b)

Figure 20. B4 strands on a quartz-feldspar vein (a) and on a quartz vein (b).

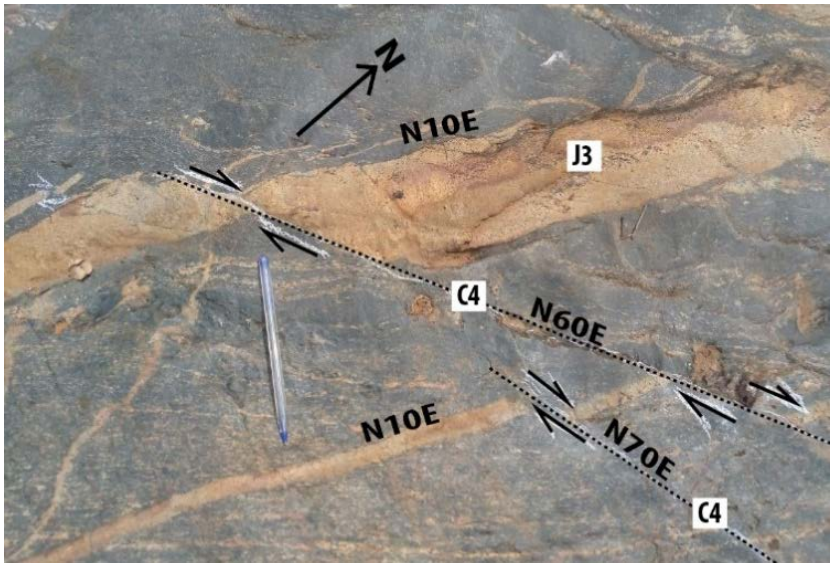

(a)

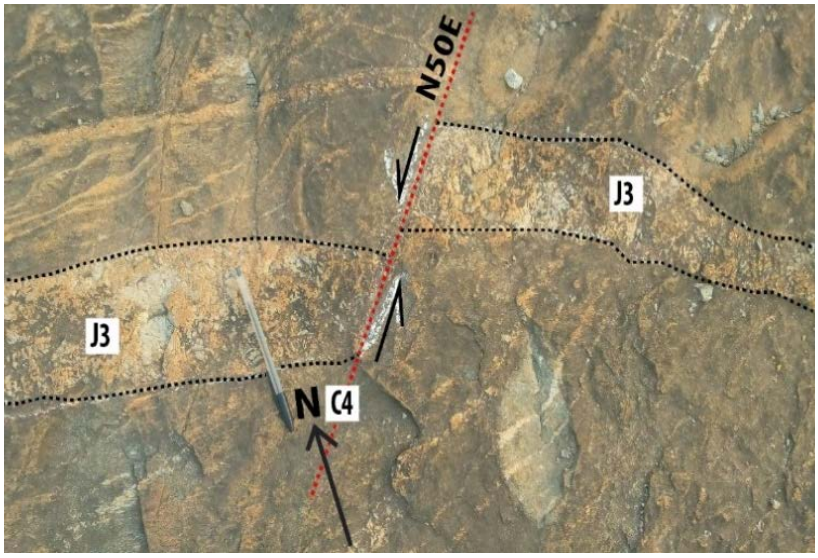

(b)

Figure 21. C4 shear affecting veins in biotite gneiss (a) and amphibole-biotite gneiss (b).

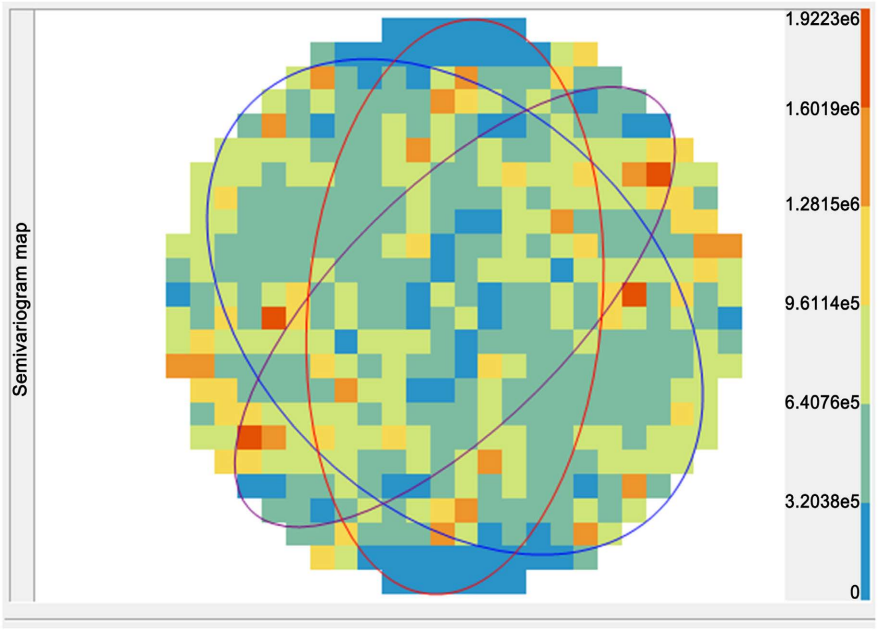

Figure 22. Tin variographic map.

the lowest variogram values. Previous studies have shown two preferential mineralization directions, N320E and N35E (Nguene, 1982). To corroborate this, structural analyses carried out in the field have given N315E, N0 and N40E as the major directions of mineralization. The map in the figure further confirms these directions with anisotropic ellipse representations: N315 in blue, N0 in red and N35 in violet. It is along these directions that the directional variograms have been constructed (**Figure 23**).

The final variogram obtained is used for the estimation neighborhood. It has the following characteristics:

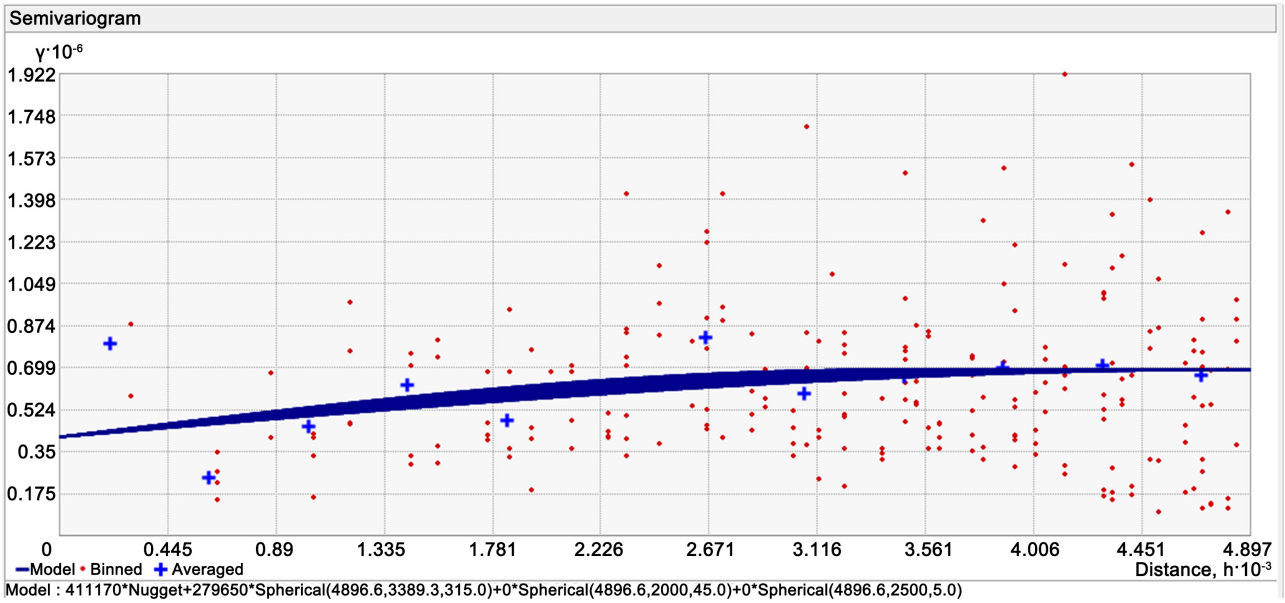

Figure 23. Directional variograms.

- A spherical model;
- A nugget effect of 279,650 ppm^2 representing sampling, analysis or localization error;
- A bearing of 411,170 ppm^2 representing the variance of the variogram;
- Two minor spans of 339 m and one major span of 590 m used as radii of the estimation ellipsoid.

The above results were used to construct a geostatistical estimator using ordinary kriging to obtain the prediction maps shown in Figures 23-25. In order to better understand certain small-value data, a conversion was made on the contents from percentage (%) to parts per million (ppm).

Figure 24 shows the spatial representation of tin grades. Three main zones of mineralization are identified:

- A low-grade zone between 0 and 1450 ppm located between the northeast and south of the study area;
- A zone of medium concentration with a grade of between 1500 and 1800 ppm in the center;
- A high-concentration zone to the northwest, with concentrations in excess of 2000 ppm.

Figure 25 shows the distribution of niobium in the study area. Values increase from west to east. Thus we have:

- A zone of low concentration between coordinates 780,000 and 788,000 in X and 712,000 and 718,000 in Y, with grades below 690 ppm;
- A zone of high concentration from the center of the map to the east, with concentrations approaching 1475 ppm.

In our study area, tantalum dispersion is predominantly low, below 300 ppm (Figure 26). Like tin, its dispersion is strong in the northeast and weak in the southwest.

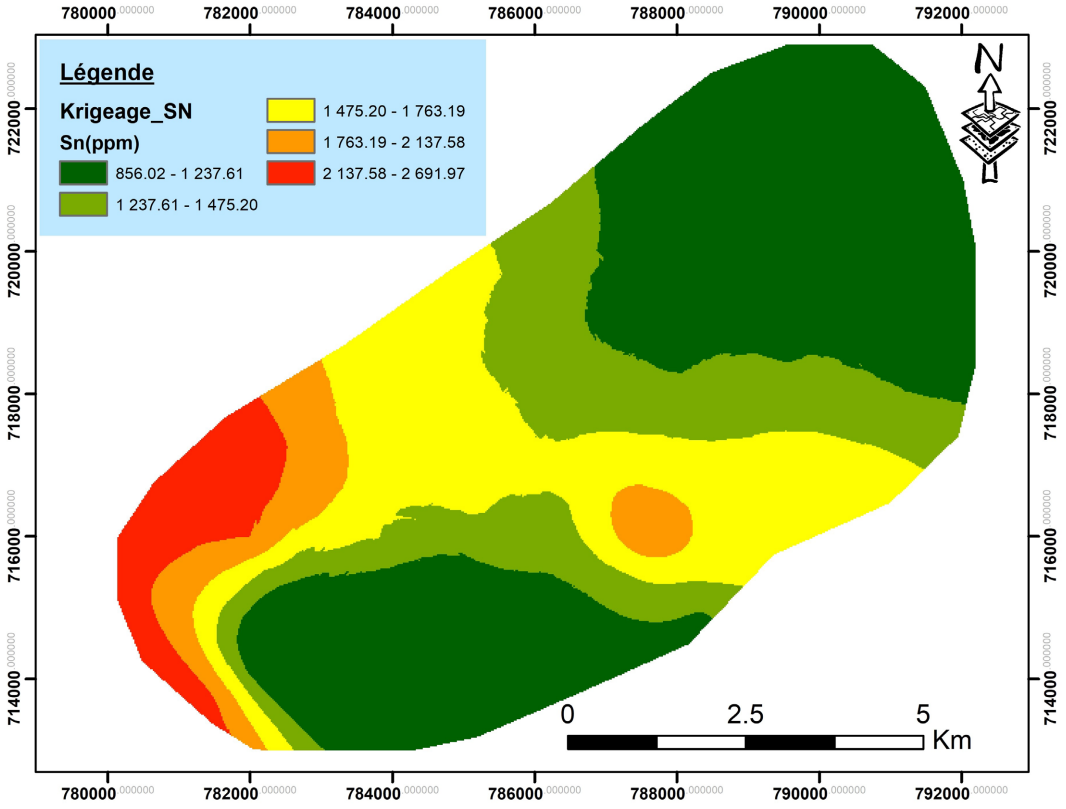

Figure 24. Tin prediction map.

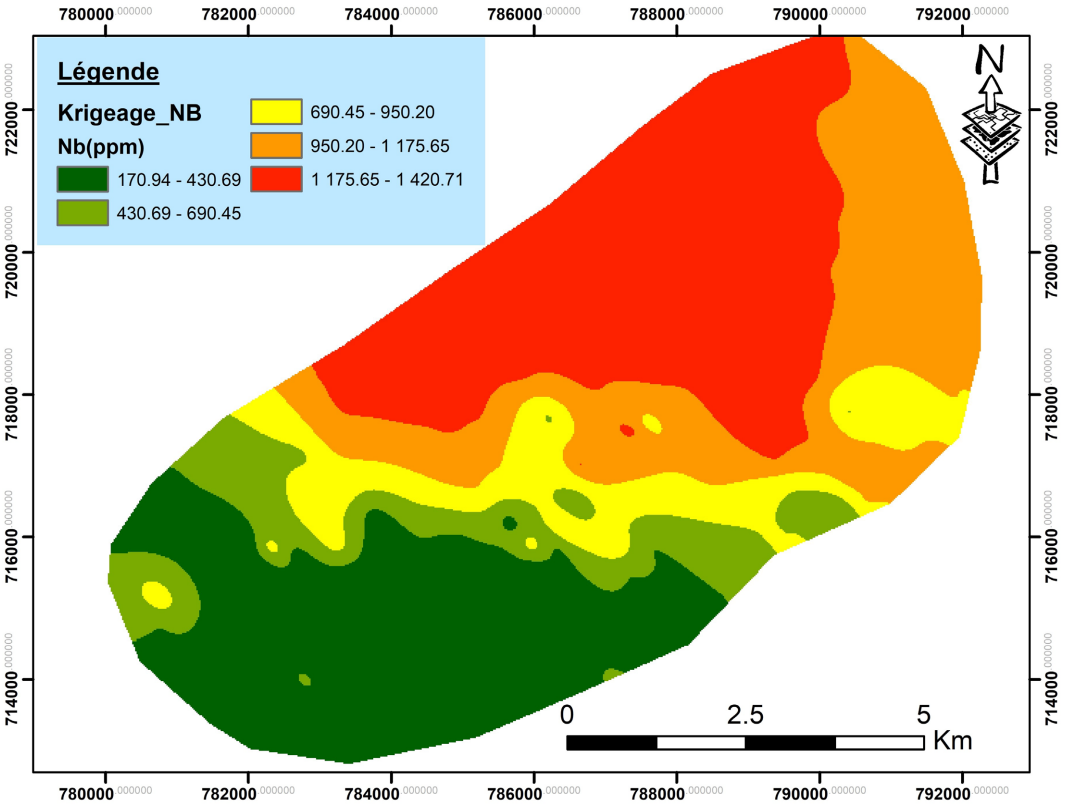

Figure 25. Niobium prediction map.

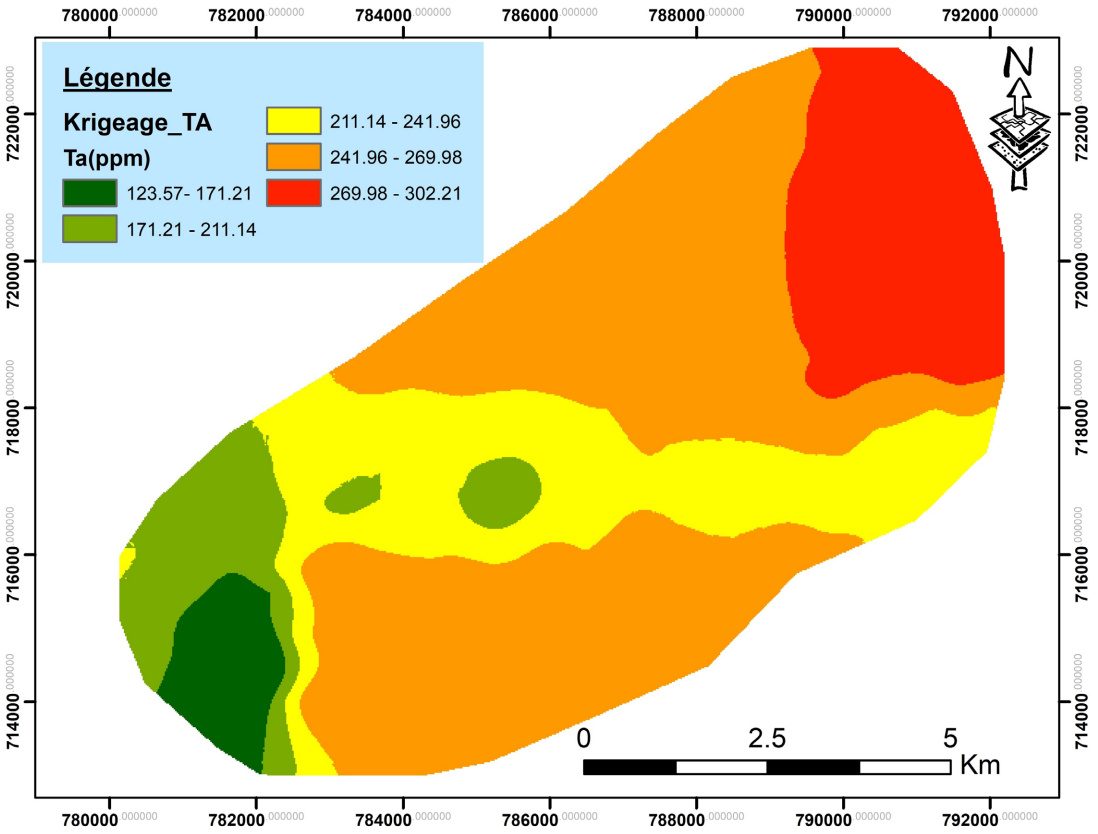

Figure 26. Tantalum prediction map.

The three maps produced show Sn, Ta and Nb concentrations in the study area. A joint synthesis of the modelling results shows:

- Confirmation of the major directions revealed by the structural study: tin, tantalum and niobium mineralization are concentrated along strike N315E to N320E, with mineralization also occurring along strike N35E for high-grade Sn, medium-grade Ta and low-grade Nb;
- Concentrations disperse progressively in space: positively from east to west for tantalum and niobium, and inversely for tin.

5. Conclusion

The study of the spatial dispersion of tin, niobium and tantalum mineralization associated with the Mayo Darlé granitoids enabled us, firstly, to draw up a sampling map highlighting the data to be used for predictive mapping; secondly, to plot histograms of Sn, Nb and Ta values after an exploratory analysis of the geochemical data and, finally, to draw up predictive maps of Sn, Nb and Ta. For the predictive maps, we used two approaches: 1) a field data approach (structural analysis) and 2) a geostatistical approach using geochemical data.

Statistical analysis of Sn values gave a mean of 0.059% and a standard deviation of 0.157%. The histogram is unimodal, with the lowest grades having the highest frequencies. The histogram of niobium values shows two main zones of

mineralization: zone 1, with niobium grades between 0.01% and 0.06%, and zone 2, with niobium concentrations above 0.2%. Over 95% of samples have a niobium content of less than 0.2%. The histogram of tantalum values highlights four main zones of mineralization: Zone 1, with tantalum grades between [0.01%; 0.012%[; zone 2 with tantalum concentrations between [0.012%; 0.014%[; zone 3 with tantalum concentrations between [0.014%; 0.018%[; zone 4 with tantalum concentrations between [0.019%; 0.025%[. 25% of samples have a tantalum content greater than 0.01. The three histograms produced follow a lognormal trend like that of gold ore (Emery, 2001).

The predictive map for tin shows three main zones of mineralization: a low-grade zone between 0 and 1450 ppm located between the northeast and south of the study area, a medium-grade zone between 1500 and 1800 ppm in the center and a high-grade zone in the northwest with concentrations above 2000 ppm. The niobium map shows a zone of low concentration between coordinates 780,000 and 788,000 in X and 712,000 and 718,000 in Y, with concentrations below 690 ppm, and a zone of high concentration from the center of the map to the east, with concentrations approaching 1475 ppm. Tantalum has a predominantly low dispersion of less than 300 ppm. Like tin, its dispersion is strong in the northeast and weak in the southwest.

Conflicts of Interest

The authors declare no conflicts of interest regarding the publication of this paper.

References

Ayiwouo, M. N., Sriram, S., Ngounouno, F. Y., Rajagopal, K., & Ngounouno, I. (2023). Assessment of the Environmental Impacts of Gold Mining Activities at Gankombol (Adamawa-Cameroon) Using Leopold Matrix, Fecteau Grid and Remote Sensing Approach. *Journal of African Earth Sciences, 207,* Article 105050. https://doi.org/10.1016/j.jafrearsci.2023.105050

Baillargeon, S. (2005). *Le krigeage: Revue de la théorie et application à l'interpolation spatiale de données de precipitations*. Mémoire, Faculté des études supérieures, Université Laval.

Barnett, V., Lewis, T. et al. (1994). *Outliers in Statistical Data*. Wiley.

Boroh, A. W., Lawou, S. K., Kuiekem, D., Langollo, Y. T., & Ngounouno, I. (2022b). Development of a 3D Variogram Using the Analytical Geometry of the Plane and Space: Application in Nkout Center Iron Deposit (South Cameroon). *Arabian Journal of Geosciences, 15,* Article No. 477. https://doi.org/10.1007/s12517-022-09802-z

BRGM (1986). *Rapport sur l'étain de Mayo Darlé*. Rapport No. 86, CMR 070.

Calder, C. A., & Cressie, N. A. (2009). Kriging and Variogram Models. In *International Encyclopedia of Human Geography* (pp. 49-55). Elsevier Science. https://doi.org/10.1016/B978-008044910-4.00461-2

Chilès, J.-P., & Delfiner, P. (2012). *Geostatistics: Modeling Spatial Uncertainty*. John Wiley & Sons, Inc. https://doi.org/10.1002/9781118136188

Déruelle, B., Ezangono, J., Lissom, J., Loulé, J.-P., Ngnotué, N., Ngounouno, I.,

Nkoumbou, C., Nono, A., & Simo, E (1987). Mio-Pliocene Basaltic Lava Flows and Phonolitic and Trachytic Plugs North and East of Ngaoundere (Adamawa, Cameroon). In C. Matheis, & A. Schandelmeier (Eds.), *Current Research in African Earth Sciences* (pp. 261-264). Balkema.

Emery, X. (2001). *Géostatistique Linéaire*. Éc. Natl. Supér. Mines Paris Cent. Géostatistique. http://cg.ensmp.fr/bibliotheque/public/EMERY_Cours_00387.pdf

Ézangono, J., Déruelle, B., & Ménard, J.-J. (1995). Benmoreites from Tchabal Djinga Volcano (Adamawa, Cameroon), Products of Kaersutite + Plagioclase Assimilation by a Trachytic Magma. *Terra Abstracts. Abstract Supplement to Terra Nova* (p. 161), Vol. 7, Wiley-Blackwell.

Gazel, J., Lasserre, M., Limasset, J.-C., & Vachette, M. (1963). Age absolus des massifs granitiques ultimes et de la minéralisation en étain du Cameroun central. *Comptes rendus de l'Académie des Sciences, 255,* 2875-2878.

Gèze B. (1941). Sur les massifs volcaniques du Cameroun occidental. *Comptes rendus de l'Académie des Sciences, 212,* 498-500.

Glacken, I., Snowden, D., & Edwards, A. (2001). Mineral Resource Estimation (pp. 189-198). In A. Edwards (Ed.), *Mineral Resource and Ore Reserve Estimation—The AusIMM Guide to Good Practice*, The Australasian Institute of Mining and Metallurgy.

Gweth, P. N. (2011). *Ressources minérales du Cameroun*. SOPECAM, Yaoundé, 375 p.

Ibrahim, A., & Al-Tamir, M. (2023). Spatial Distribution Prediction for the Ground Water Quality in Mosul City (Iraq) Using Variogram Equations. *Scientific Review Engineering and Environmental Sciences (SREES), 32,* 186-197. https://doi.org/10.22630/srees.4583

Kampunzu, A. B., & Popoff, M. (1991). Distribution of the Main Phanerozoic African Rifts and Associated Magmatism: Introductory Notes. In A. B. Kampunzu, & R. T. Lubala (Eds.), *Magmatism in Extensional Structural Settings. The Phanerozoic African Plate* (pp. 2-10). Springer-Verlag. https://doi.org/10.1007/978-3-642-73966-8_1

Laplaine, L. (1969). Indices minéraux et ressources minérales du Cameroun. *Bulletin de la Direction des Mines et Géologie, No. 5*. 63-73.

Lasserre, M. (1978). Mise au point sur les granitoïdes dits "ultimes" du Cameroun: Gisement, pétrographie et géochronologie. *Bulletin Bureau Recherches Géologiques Minieres, 4,* 143-159.

Maharana, K., Mondal, S., & Nemade, B. (2022). A Review: Data Pre-Processing and Data Augmentation Techniques. *Global Transitions Proceedings, 3,* 91-99. https://doi.org/10.1016/j.gltp.2022.04.020

Moreau, C., Regnoult, J.-M., Déruelle, B., & Robineau, B. (1987). A New Tectonic Model for the Cameroon Line, Central Africa. *Tectonophysics, 139,* 317-334. https://doi.org/10.1016/0040-1951(87)90206-X

Ngounouno, I. (2013). *La Pétrologie Eruptive Moderne (Tom 2). Le Cameroun, l'Islande, les Andes*. L'Harmattan.

Nguene, F. R. (1982). *Geology and Geochemestry of the Mayo-Darlé Tin Deposit, West-Central Cameroon, Central Africa*. Doctor of Philosophy in Earth Resources, New Mexico Institute of Mining and Technology.

Nkouandou, O. F. (2006). *Pétrologie du volcanisme cénozoïque au nord et à l'est de Ngaoundéré (Adamaoua, Cameroun)*. Thèse Doct., Univ. Pierre et Marie Curie, 105 p.

Nono, A., Déruelle, B., Demaiffe, D., & Kambou, R. (1994). Tchabal Nganha Volcano in Adamawa (Cameroon): Petrology of a Continental Alkaline Lava Series. *Journal of*

Volcanology and Geothermal Research, 60, 147-178.
https://doi.org/10.1016/0377-0273(94)90066-3

Reza, S., Baruah, U., Sarkar, D., & Das, T. (2010). Evaluation and Comparison of Ordinary Kriging and Inverse Distance Weighting Methods for Predication of Spatial Variability of Some Chemical Parameters of Dhalai District, Tripura. *Agropedoiogy, 20,* 38-48.

Rossi, M. E., & Deutsch, C. V. (2013). *Mineral Resource Estimation*. Springer Science & Business Media. https://doi.org/10.1007/978-1-4020-5717-5

Appendices

				%			
Samples	X	Y	Z	Nb	Sn	Ta	Sn/Nb + Ta
MDM01	789,844	717,750	1250	0.01	0	0.02	0.00
MDM02	789,835	718,268	1248	0.01	0.32	0.01	16.00
MDM03	789,943	717,801	1240	0.01	0	0.01	0.00
MDM04	781,184	713,971	1330	0.03	0.03	0.02	0.60
MDM05	781,396	713,781	1350	0.03	0.02	0.01	0.50
MDM06	781,058	713,698	1352	0.03	0.06	0.01	1.50
MDM07	780,850	713,464	1320	0.03	0	0.02	0.00
MDM08	781,519	714,260	1300	0.03	0.02	0.01	0.50
MDM09	780,989	714,419	1303	0.03	0.03	0.01	0.75
MDM10	782,830	715,903	1215	0.01	0.06	0.01	3.00
MDM11	782,760	715,873	1230	0.01	0.01	0.01	0.50
MDM12	782,609	715,986	1226	0.01	0.04	0.01	2.00
MDM13	782,824	715,923	1227	0.01	0.01	0.01	0.50
MDM14	782,854	715,873	1224	0.01	0.07	0.01	3.50
MDM15	782,706	715,985	1228	0.01	0.05	0.01	2.50
MDM16	782,690	715,966	1228	0.01	0.05	0.01	2.50
MDM17	782,730	715,962	1230	0.01	0.04	0.01	2.00
MDM18	782,668	716,044	1220	0.01	0.07	0.01	3.50
MDM19	781,951	716,441	1206	0.01	0.05	0	5.00
MDM20	782,706	716,003	1205	0.02	0.11	0.02	2.75
MDM21	782,931	716,498	1228	0.04	0.012	0.01	0.24
MDM22	782,947	716,399	1230	0.04	0.11	0.01	2.20
MDM23	782,854	716,430	1202	0	0	0	0.00
MDM24	782,888	716,377	1250	0.01	0.01	0.01	0.50
MDM25	782,496	715,879	1230	0.04	0.06	0.01	1.20
MDM26	782,740	715,967	1227	0.04	0.03	0.01	0.60
MDM27	782,520	715,831	1233	0.04	0	0.01	0.00
MDM28	782,618	715,771	1231	0.01	0	0.01	0.00
MDM29	781,212	715,651	1300	0.02	0.01	0.01	0.33
MDM30	781,211	715,594	1320	0.02	0.07	0.01	2.33
MDM31	782,908	716,406	1216	0.02	0.19	0.02	4.75
MDM32	782,674	716,394	1183	0.03	0	0.02	0.00
MDM33	783,227	716,420	1195	0.02	0	0.01	0.00
MDM34	782,002	716,072	1215	0.02	0.01	0.02	0.25
MDM35	782,065	715,994	1225	0.02	0.11	0.02	2.75
MDM36	782,081	715,905	1225	0.02	0.19	0.01	6.33
MDM37	781,989	715,974	1219	0.02	0.19	0.02	4.75

Continued

MDM38	781,252	715,634	1250	0.03	0.26	0.02	5.20
MDM39	781,253	715,572	1235	0.03	0.14	0.02	2.80
MDM40	783,179	715,626	1200	0.02	0	0.01	0.00
MDM41	783,231	715,496	1203	0.02	0	0.02	0.00
MDM42	783,542	715,604	1198	0.03	0	0.02	0.00
MDM43	781,183	715,580	1195	0.03	0	0.01	0.00
MDM44	781,385	715,754	1198	0.03	0	0.02	0.00
MDM45	781,347	715,269	1190	0.02	0.11	0.02	2.75
MDM46	781,708	715,564	1205	0.02	0	0.02	0.00
MDM47	783,243	715,620	1224	0.02	0.02	0.02	0.50
MDM48	783,005	715,628	1214	0.02	0.01	0.02	0.25
MDM49	782,575	715,877	1175	0.02	0.11	0.02	2.75
MDM50	783,467	716,151	1203	0.01	0	0.01	0.00
MDM51	782,017	716,257	1243	0.01	0	0.01	0.00
MDM52	782,701	715,886	1228	0.01	0	0	0.00
MDM53	782,305	716,180	1242	0	0	0.01	0.00
MDM54	781,645	715,846	1197	0.01	0	0	0.00
MDM55	781,357	715,703	1240	0.01	0.01	0.01	1.00
MDM56	782,638	716,511	1236	0.01	0.01	0	1.00
MDM57	782,274	715,261	1268	0.01	0	0.02	0.00
MDM58	782,984	716,468	1198	0.02	0.01	0.01	0.33
MDM59	782,844	716,494	1205	0.02	0.04	0.02	1.00
MDM60	783,031	716,419	1195	0.02	0	0.02	0.00
MDM61	781,353	713,947	1405	0.01	0.11	0.01	5.50
MDM62	781,295	713,982	1392	0.02	0.18	0.01	6.00
MDM63	781,256	714,001	1385	0.02	0.01	0.01	0.33
MDM64	781,399	713,915	1416	0.03	0.01	0.01	0.25
MDM65	781,353	713,946	1405	0.03	0.24	0.01	6.00
MDM66	781,419	713,867	1410	0.03	0.01	0.01	0.25
MDM67	781,295	713,982	1392	0.03	0.03	0.01	0.75
MDM68	781,494	713,930	1449	0.03	0.02	0.01	0.50
MDM69	781,516	713,870	1440	0.03	0.02	0.01	0.50
MDM70	782,686	716,082	1250	0.01	0	0.01	0.00
MDM71	782,663	715,994	1230	0.01	0.04	0.01	2.00
MDM72	782,708	715,898	1233	0	0	0.01	0.00
MDM73	782,781	715,806	1220	0.01	0.05	0.01	2.50
MDM74	782,843	715,880	1224	0.01	0.04	0.01	2.00
MDM75	782,749	715,823	1223	0.01	0.01	0.01	0.50
		Average grade %				**0.019**	**0.047** **0.011**
		Average quantity %				**25%**	**61%** **15%**